Probability-weighted ensemble support vector machine for intelligent recognition of moving wear debris from joint implant

Yeping Peng [a], Hongtao Yue [a], Song Wang [b], Guangzhong Cao [a,*], Hongkun Wu [c,*], Chaozong Liu [d]

[a] *Guangdong Key Laboratory of Electromagnetic Control and Intelligent Robots, College of Mechatronics and Control Engineering, Shenzhen University, Shenzhen 518060, China*
[b] *Biomechanics and Biotechnology Lab, Research Institute of Tsinghua University in Shenzhen, Shenzhen 518057, China*
[c] *School of Mechanical and Manufacturing Engineering, The University of New South Wales, Sydney, NSW 2052, Australia*
[d] *Institute of Orthopaedics and Musculoskeletal Science, University College London, Royal National Orthopaedic Hospital, London HA7 4LP, UK*

A B S T R A C T

Friction-induced wear debris from joint implants are effective resources in investigating artificial joint wear and cellular immune response mechanisms. To improve the accuracy of wear debris analysis, an intelligent recog- nition method is developed for wear debris measurement under motion conditions. In this method, the multi- view image sequence of moving wear debris is captured to acquire the variations of aspect ratio, area, and roundness features. Then multiple SVM models are integrated to identify wear debris types based on weighted probability to improve the accuracy. The proposed method can achieve a classification accuracy of 90.51%, which is better than HIVE-COTE2.0, MultiRocket, and other time series classification algorithms. This method can be applied to monitor wear status of artificial joint articulating surfaces.

1. Introduction

The artificial joint implanted in the human body will generate a large amount of wear debris due to the articulating motion. This process is regarded as a potential risk that will accelerate joint deterioration and induce biochemical reactions within cells, which can cause inflammation, joint disease, and joint failure [1]. Therefore, the analysis of those wear debris is becoming an important method to investigate the wear mechanisms of artificial joint wear and the pathogenesis of wear debris caused disease [2,3]. Since different wear stages will produce different types of wear debris, the associated impacts on joint wear and risks to patients also vary. Extracting the quantities and morphological characteristics of wear debris, and examining their types could provide crucial information on the wear process developed inside the patient's body [4–6].

To extract wear debris information, many image identification algorithms have been developed [7–9] in which image-based ferrography is most typical [10–12]. A WP-DRnet ferrography image classification network [13] was proposed to detect wear debris by integrating two convolutional neural networks (CNNs). Another feature fusion-based debris recognition network FFWR-Net was developed [14], which fuses the features extracted by deep learning and manual intervention, to identify five debris types such as cutting, fatigue, sphere, non-metal, and sliding. Another recognition method built on CNN and transfer learning (TL) can effectively identify cutting, stick, and fatigue wear debris [15]. An Inception-v3 model was also reported to address the overlapping problem in ferrography [16]. A CNN with three classifiers was developed to determine the fatigue, oxide, and spherical wear debris. Due to the small size, the scanning electron microscope (SEM) is often used to collect images of artificial joint wear debris. The morphological features such as equivalent circle diameter and aspect ratio then can be extracted for debris shape recognition. On this basis, logistic regression was applied to classify flake, fibrous, and granular artificial joint wear debris [4]. An automatic morphological residual convolutional neural network (M-RCNN) was also proposed [17] to identify flake, sphere, and band-like debris types. It should be noticed that the above-mentioned recognition algorithms are mainly applied for static wear debris and single-view identification. However, because the single-view image cannot provide comprehensive shape information, it is easy to produce errors in identifying irregular-shaped wear debris.

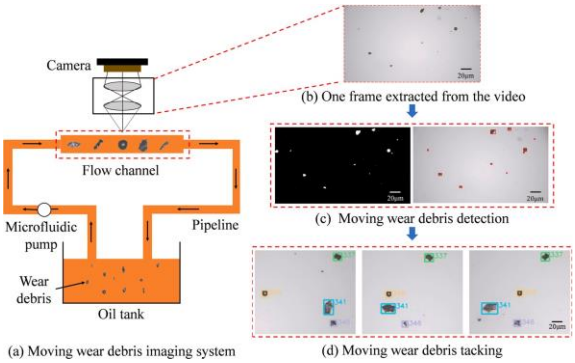

Fig. 1. Schematic diagram of the moving wear debris imaging system.

To improve the accuracy of identifying irregular-shape wear debris, many recognition algorithms with multi-view image sequences were developed [5,18–20]. With the captured image, two-dimensional features of different angles are extracted to construct the three-dimensional representation of wear debris. A micro-channel video acquisition system can make use of hydrodynamic properties to keep the debris rolling. A microscope can then be used to capture multi-view images of the rotating wear debris [21]. The profile parameters of aspect ratio and equivalent circle diameter were extracted and used to construct three-dimensional features [22]. On this basis, an online wear debris identification method was reported, which integrates multi-information including three-dimensional features and colour features, and combines SVDD multi-classifier with K-means clustering and SVM classifier [23]. In addition, the decision tree dynamic identification model of "three layers and six elements" was formulated that allows online identification of wear debris against various mechanisms such as oxidation, cutting, and fatigue. To improve the accuracy of 3D feature extraction, a multi-view image sequence was also incorporated, whereby moving wear debris were detected and tracked to reconstruct their 3D models [19]. In another approach, structure from motion (SfM) and shape from shading (SfS) were used to achieve the sparse and dense reconstruction of debris surfaces, respectively [18,24]. The results show that those methods can reconstruct the wear debris at various angles and the error of the regional characterization parameters is less than 20%. Moreover, the three-dimensional (3D) surface of wear debris was also reconstructed through multi-view contour fitting and dense point cloud interpolation to obtain comprehensive features for wear debris analysis [20].

Although preliminary progress has been made in the research on wear debris identification, recognition of irregular debris under motion conditions is still rarely touched. Furthermore, debris adhesion may occur during their movements, which will lead to errors in wear debris feature extraction and recognition. In addition, the number of wear debris is often large, and it takes a long time to obtain their three-dimensional features by merely relying on 3D reconstruction. Especially, in the field of artificial joint wear debris analysis, efficiency is preferred but there is limited attention to real-time monitoring. To develop a new real-time dynamic recognition algorithm, a moving wear debris identification method based on dynamic feature fusion is introduced in the current work. Firstly, detection and tracking of the moving wear debris to locate the target objects in different image frames are conducted to obtain the multi-view image sequences [20,21,25]. After that, the variation curves of debris area, aspect ratio, and roundness features are extracted from the image sequence. To distinguish four wear debris types from block, stick, sphere, and flake according to changes in the characteristic curve, it is needed to further extract the feature vector to represent the properties of the whole curve, where three SVM classifiers are utilised. Finally, the classification results of the three SVM models are fused to determine the type of wear debris.

The rest of this paper is organised as follows. The moving wear debris video acquisition system is introduced in Section 2. Section 3 contains the description of the cycle calculation and feature selection processes of the wear debris characteristic curve. Section 4 presents the wear debris classification method based on the weighted probability integrated SVM algorithm. The experiment and comparative results are described and discussed in Section 5. The conclusion is drawn in Section 6.

2. Video acquisition of moving wear debris

To obtain multi-view observations of moving wear debris, a moving wear debris imaging system is utilised and the schematic diagram is shown in Fig. 1 [20,21]. It includes three main modules: video acquisition, moving wear debris detection, and moving wear debris tracking. The video acquisition module (Fig. 1(a)) composes of an oil tank, a microfluidic pump, a flow channel, and a camera. When the system is working, the microfluidic pump provides a stable flow rate of 30 ml/h and flushes the wear debris into the flow channel. When the wear debris passes through the field of view of the camera, the videos are captured with the frame rate of 30 fps (frame per second). The image resolution is 2736×1824 pixels. Fig. 1(b) shows one frame extracted from the video. The width of the field of view is 1332.45 μm.

In the motion detection module, the background of the video is established by the Gaussian mixture model (GMM) [26], then the moving wear debris are detected by background difference, as shown in Fig. 1(c). To acquire a multi-view image sequence of irregular shapes, debris tracking is required. In this work, the deep-sort method [27] is applied for moving debris tracking. The cascade matching algorithm is composed of Kalman filtering and the Hungarian algorithm to reduce the tracking error caused by object occlusion. An example of the moving wear debris tracking process can be seen in Fig. 1(d). In the figure, the number in the upper right corner is the identity (ID) index labelling the tracked wear debris.

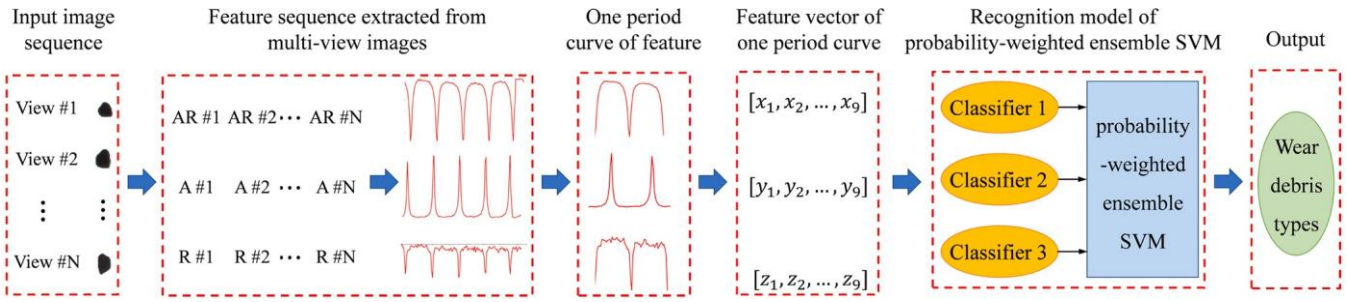

Fig. 2. The flowchart of moving wear debris recognition.

Table 1
Characteristic parameters of a periodic curve.

Index	1	2	3	4	5
Feature	Mean	Variance	Standard deviation	Maximum	Minimum
Index	6	7	8	9	
Feature	Coefficient of variation	Sample skewness	The length of the longest continuous subsequence below the mean value	The length of the longest continuous subsequence above the mean value	

After the detection and tracking of moving wear debris, the image sequence under different viewing angles can be captured. It can be seen in Fig. 1(d) that the images of the same debris from different view angles show different profiles and morphological features. This indicates that multi-view image sequences can avoid the identification errors of irregular wear debris such as block and flake debris. It needs to be mentioned that the wear debris is extracted from the lubricants, such as normal saline, bovine serum, and PBS powdered, and then is dried to prepare oil samples with lubricating oil. This is to avoid the influences of different lubricants on wear debris image acquisition. Based on this imaging system, a moving wear debris recognition method is developed based on the captured multi-view image sequence and is introduced in the next section.

3. Moving wear debris recognition method based on multi-view image sequence

Fig. 2 is the flowchart of the proposed method for moving wear debris recognition. Given the multi-view image sequence as input, the debris features including aspect ratio, roundness, and area, are first extracted from each frame. Characteristic variation curves are obtained that indicate the change of extracted features of the multi-view appearance of a tracked wear debris. Then the period of the characteristic change curve is estimated using autocorrelation, whereby a single period curve is generated. For the overall feature variation trend, the feature vector of each debris includes nine features (see Section 3.3, Table 1). Finally, a recognition model based on probability-weighted ensemble SVM is built to identify irregular wear debris.

3.1. Extraction of multi-view feature sequences of wear debris

During the wear processes of artificial joint, abrasive wear commonly produces stick-like wear debris. Block- and flake-like wear debris is generally generated from fatigue wear process. In the adhesive wear stage, irregular block wear debris can be found. Correspondingly, four types of wear debris, block, stick, sphere, and flake, are often detected and recognized to analyse the wear mechanisms of artificial joints.

In Fig. 3, ten viewing frames of each debris are displayed. It can be seen that the contours of the block-shaped wear debris are mostly irregular at different viewing angles; the stick-shaped debris are slender and have a large aspect ratio; the spherical debris are often showing circular or quasi-circular contours with greater roundness. The profiles of flake wear debris are more complex, suggesting that are irregular features in blocks, elongation sticks, and sphere-like circles shapes simultaneously in different viewing angles.

Wear debris features are extracted from every image of different viewing angle to acquire the characteristic change curve. To incorporate the feature information from different profiles for effective recognition, area (A), aspect ratio (AR), and roundness (R) are selected to describe the changes. This is because the variation of aspect ratio and roundness is related to the debris types, especially for distinguishing stick and spherical wear debris, as shown in Fig. 4. It also can be seen from Fig. 4

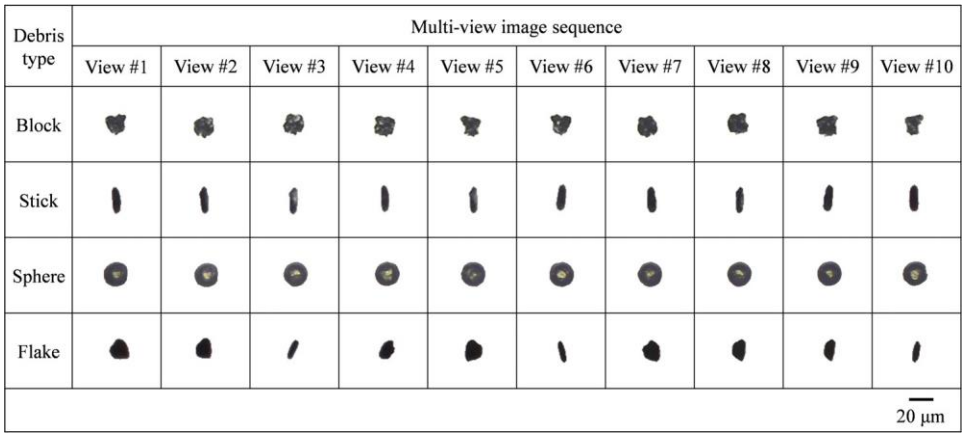

Fig. 3. Four common types of wear debris that are detached from artificial joints.

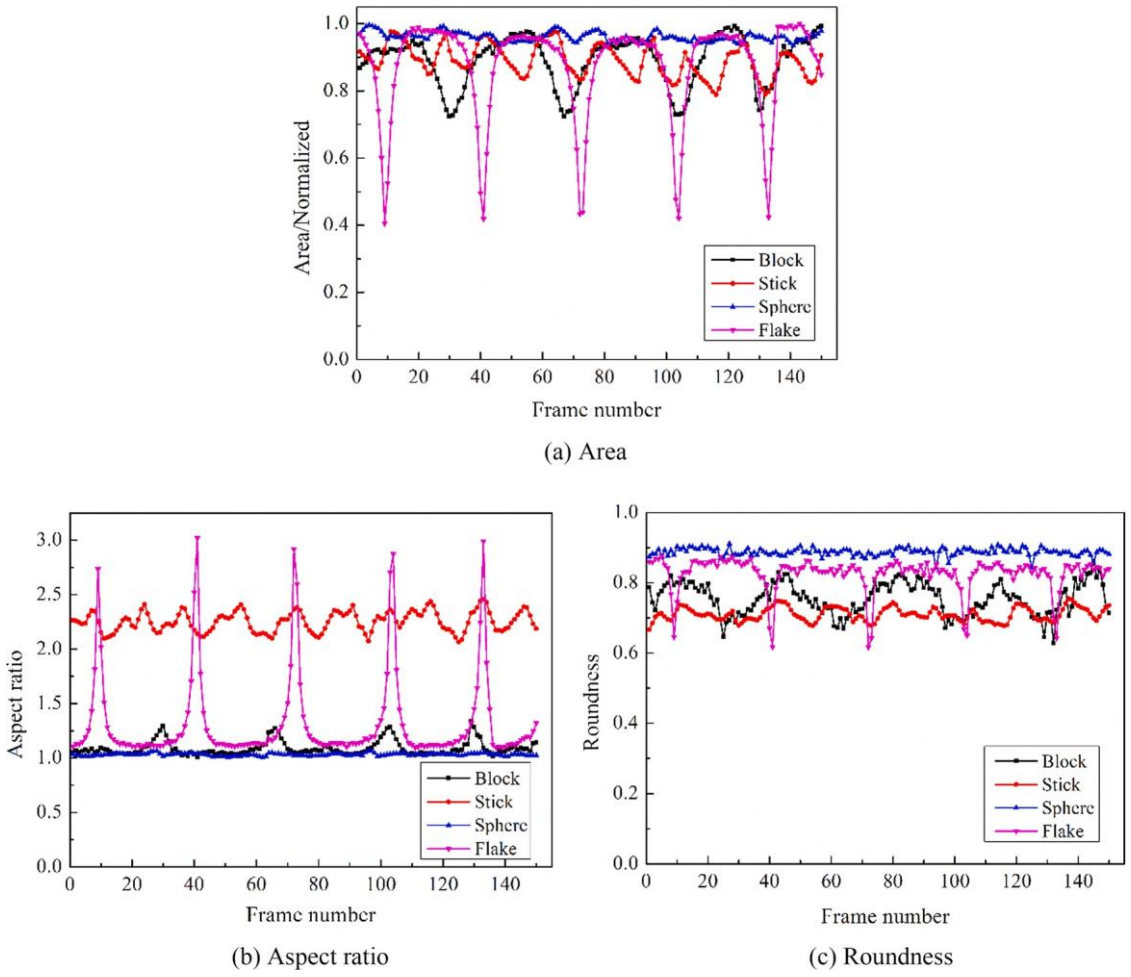

Fig. 4. The feature curves of four types of wear debris shown in Fig. 3.

that the debris area is strongly correlated with the size and contour shape, and the flake-like debris can be quickly distinguished by the area change at different viewing images. The three characteristic parameters are calculated as follows:

$$A = \lambda \sum_{i=0} \sum_{j=0} f(i,j) \tag{1}$$

$$AR = \frac{L}{W} \tag{2}$$

$$R = \frac{4A\pi}{P^2} \tag{3}$$

where x-y is the pixel coordinate, $f(i, j)$ is the pixel value in the binary image of wear debris, $f(i, j) = 1$ when the pixel is located in the debris region; otherwise, $f(i, j) = 0$; $\lambda$is the actual area of a pixel, L is the larger dimension of the smallest rectangle enclosing the debris profile, W is the smaller dimension of the smallest rectangle, and P is the debris contour perimeter.

In Fig. 4, the area values are normalized by Eq. (1) to eliminate the influence of wear debris sizes during shape recognition, which is also compatible with the feature fusion with non-dimensional parameters of aspect ratio and roundness.

$$X_{\text{nor}} = \frac{X}{X_{\max}} \tag{4}$$

where $X = (x_1, x_2, \ldots, x_n)$ is the feature value sequence, $X_{\max}$ is the maximum value in the sequence, and X_{nor} is the normalized feature sequence.

It can be seen from Fig. 4(a) that, for flake debris, the magnitude variation of the area between different viewing angles is larger than the other three types. In contrast, the area change of spherical debris is more stable. In Fig. 4(b), the aspect ratio curve of flake debris changes dramatically, while the curve of spherical debris smoothly changes around 1. Besides, the aspect ratios of stick debris in all viewing angles are larger than 1. For the roundness characteristics shown in Fig. 4(c), the spherical and stick-shaped wear debris changes are less than that of the flake and block debris.

3.2. *Single-cycle characteristic change curve extraction*

Wear debris rotates in the flow chip due to laminar flow [20], so the debris feature curve shows a periodic trend. It can be seen from Fig. 4 that the periodicity of flake, block, and stick wear debris is more noticeable than that of spherical ones. During the acquisition of the wear debris video, although the flow rate and the camera frame rate are constant, the speed of the wear debris varies due to its size and contour shape. The number of image frames of various debris can be different, which leads to different variation ranges and number of cycles in the feature sequences.

It also can be seen from Fig. 4 that different debris types have different number of frames in one rotation cycle. To eliminate the influence of different periods on the feature curve, the characteristic of a single period is extracted because of similar characteristics between different periods. To this end, the period of the characteristic sequence

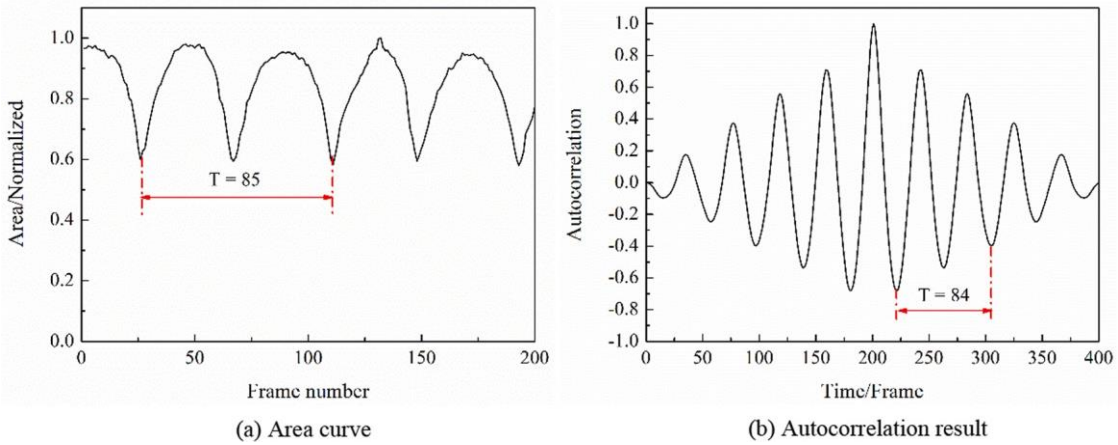

Fig. 5. Periodicity calculated from autocorrelation.

needs to be specified. Commonly used methods are Fourier transform [28] and the autocorrelation function [29]. Fourier transform is suitable for frequency domain analysis of arbitrary waveforms and has been widely used in many fields such as signals, images, and mathematics. The frequency approximation corresponding to the waveform with the largest variation amplitude can be selected to estimate the period of the time domain sequence. However, other waveforms with smaller amplitudes are also part of the time series and there are many of them, ignoring them directly will cause a large error in estimating the period.

The autocorrelation function is the cross-correlation between a sequence and itself at different points in time and is often used to analyse time-domain signals. It can be used to describe the degree of similarity or correlation between a signal and itself at different times, which is defined as

$$R_{xx}(m) = \sum_{k=-\infty}^{\infty} x(k)x(k+m) \tag{5}$$

where $x(k)$ is discrete-time signal sequence and m is the shift between two signals.

When the correlation is strong, a peak appears in $R(xx)(m)$. Therefore, the period of the original curve can be indicated by the interval between the extreme values in the autocorrelation sequence. Here, the autocorrelation function is used to calculate the period of the wear debris characteristic curve. Fig. 5(a) shows the area variation of block-shaped wear debris, which has obvious periodic characteristics. The frame number of one period is $T = 85$ manually counted according to the mirror image feature of rotating wear debris. Its corresponding autocorrelation result is shown in Fig. 5(b). The period is 84, which is only 1 unit away from the manually counting result.

3.3. Extraction of feature vector from single-cycle characteristic change curve

According to the characteristic changes, different types of wear debris may have similar feature curves. For instance, the aspect ratios of block and stick debris are similar. To effectively distinguish the wear debris, the debris features are extracted from the single-cycle characteristic change curve. Accordingly, nine features are selected to form a feature vector to describe the distribution of the debris features, as shown in Table 1.

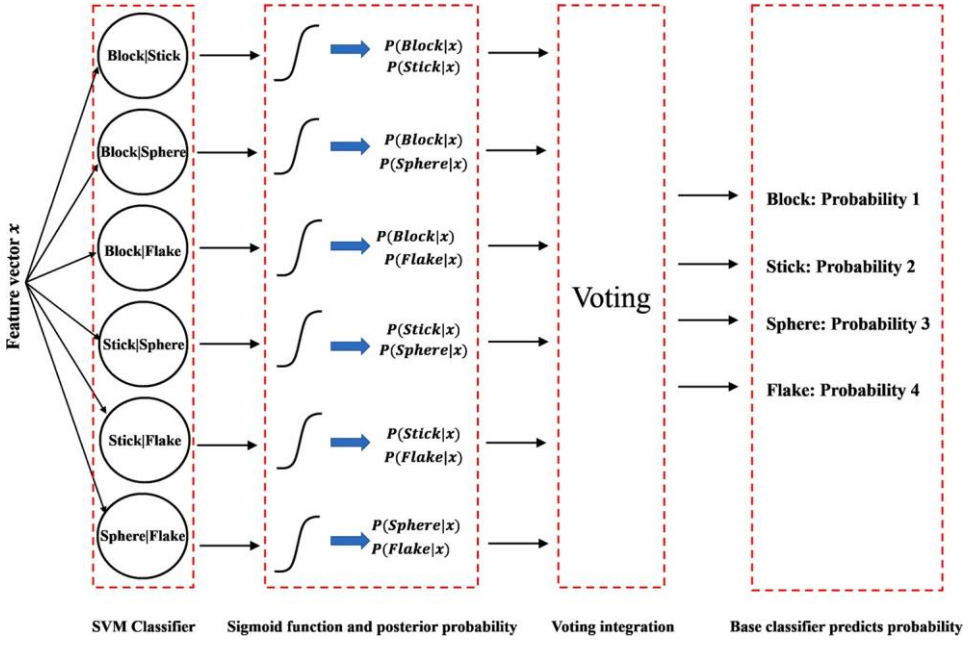

Fig. 6. Schematic diagram of the base SVM classifier for wear debris recognition.

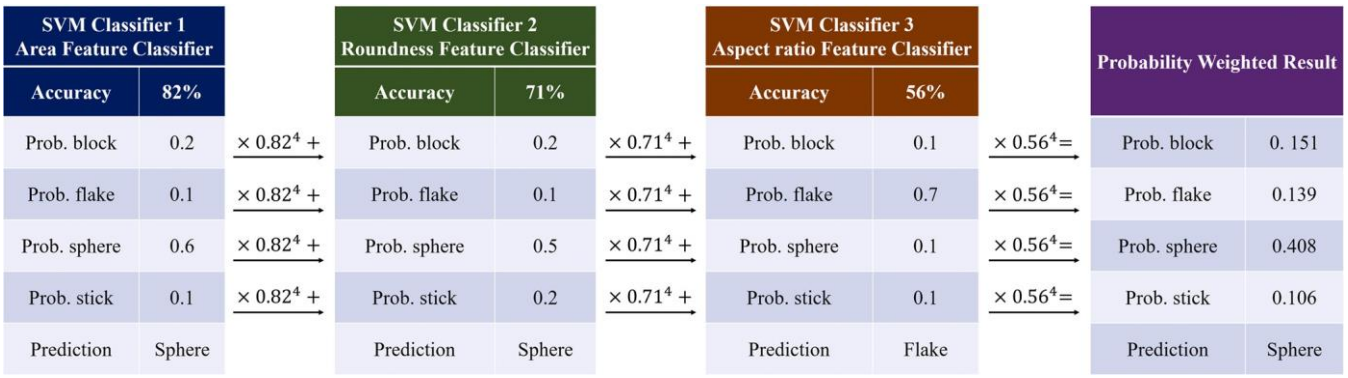

Fig. 7. Integrated classifier for dynamic recognition of wear debris.

3.4. *Wear debris recognition by probability-weighted ensemble SVM*

Fig. 4 shows that different types of wear debris have different features. Erroneous identification can be caused if only one feature is used to identify irregular debris. Thus, it is necessary to fuse multiple features (area, aspect ratio, and roundness) to recognize moving wear debris. A base classifier is trained for the recognition of each feature, and then the prediction results of the three base classifiers are fused using the weighted probabilistic ensemble method [30] to identify the wear debris types.

There are many feature classifiers available for this purpose, such as SVM, Bayesian, and decision tree. Among them, SVM finds the hyperplane to distinguish different types and is suitable for small sample classification. Hence, SVM is used to construct the base classifier of wear debris. In order to extend SVM for multiple-class classification, "one vs one" and "one vs rest" methods are commonly used [31]. The "one vs rest" method is easy to cause sample imbalance, and the training time is long, whereby the "one vs one" method is selected here to build the model as shown in Fig. 6. The input vector can be the aspect ratio, area, or roundness. Thus, a total of six SVM models are built to identify four types of wear debris, including block, stick, sphere, and flake.

Since there are six sets of SVM classification outputs from the base classifier, it is necessary to map the output of each SVM to the posterior probability [32], and then calculate the weighted distribution through the Voting module block. The probability of each type is determined, and the one with the highest probability is regarded as the final output of wear debris type.

The Voting module, shown in Fig. 6, fuses the output probability values of the six SVM classifiers. The pairwise coupling method [33] and the voting method [34] are commonly used. However, the pairwise coupling method needs to be combined with an optimization algorithm to solve the optimal value, which is not ideal for real-time identification. The voting method is simple to calculate and runs faster, and is calculated from:

$$P(i|x) = \frac{\sum_{j=1, j\neq i}^{N} P_{ij}(i|j;x)}{\sum_{k=1}^{N} \sum_{j=1, j\neq k}^{N} P_{kj}(k|j;x)}, \quad i = 1, 2, ., N \tag{6}$$

where $P_{ij}(i|j;x)$ represents the probability that the sample x is classified to the i-th class when the classifier is trained by the i-th and the j-th classes samples.

According to Eq. (6), the probability of wear debris in each category can be predicted, and the maximum probability is taken as the output result. Since the multi-view image features include area, aspect ratio, and roundness, it is necessary to establish three base classifiers. An integrated classifier is established to incorporate the identification results of the three features, as shown in Fig. 7. The weighted probabilistic ensemble method [30] based on cross-validation has been shown to be an effective classifier ensemble method.

Table 2
The sample distribution of different wear debris types.

Type	Block	Stick	Sphere	Flake	Overall
Training samples	163	162	166	169	660
Testing samples	89	26	11	32	158

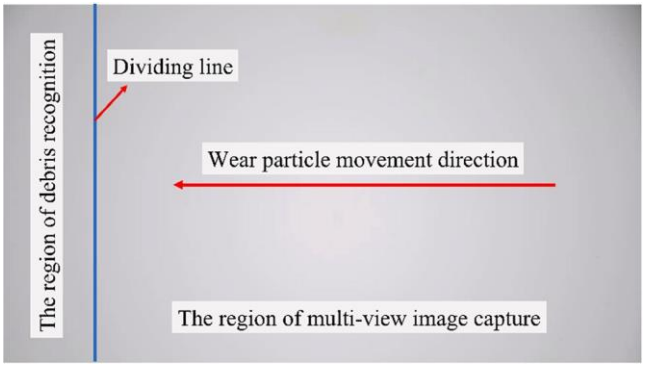

Fig. 8. The monitor system interface of moving wear debris.

It can be applied in time series classification, so it is selected as the ensemble method. The method first performs cross-validation on each base classifier in the training data and then obtains the probability output of each base classifier. Finally, the weighted fusion of the prediction results is performed to obtain the final wear debris recognition. To determine the weighted exponent parameter, the classification accuracy of different power series can be compared and assess the statistical results [30]. For the dataset obtained in our experiment, the identification accuracy of wear debris was the highest when the order of the power series is 4.

4. Experiments and discussion

4.1. *Sample data*

Experiments of ball-on-disc friction pairs under reciprocation motion were carried out to collect wear debris samples. The friction pairs were made of artificial joint materials. The balls were prepared using stainless steel, and the disks were made of Ti6Al4V. To simulate the motion conditions of joint implant, the sliding frequency was set to 2 Hz, and the stroke was 4 mm [35,36]. However, most of the produced wear debris in the sliding modes are flake-like types. Hence, the four kinds of wear debris were manually collected from different experiments to avoid the influence of imbalance data on the effeteness of classifier training. A total of 660 collected samples were manually labelled for

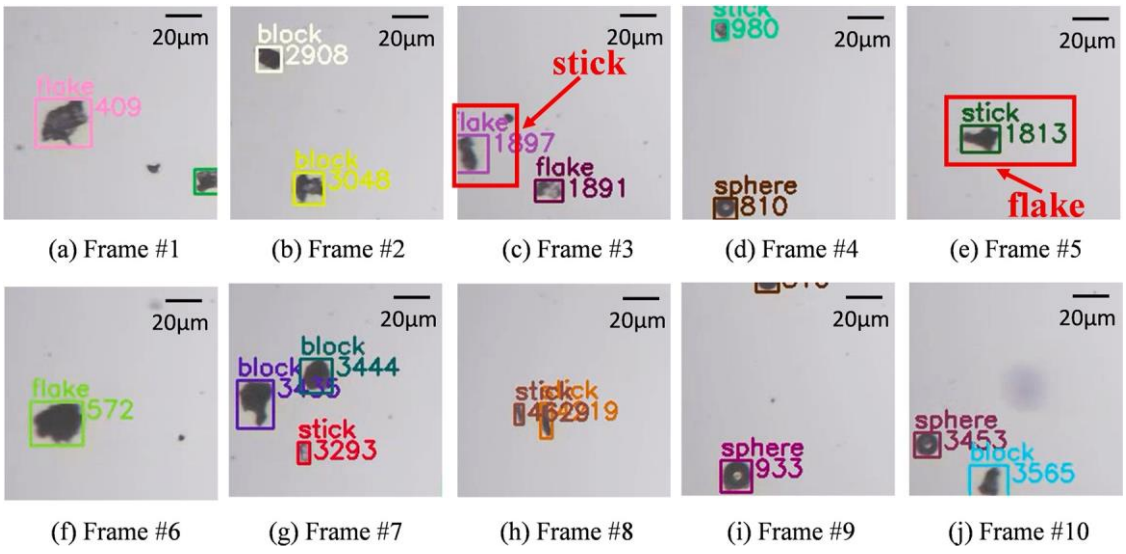

Fig. 9. Recognition results of the Inception Time method.

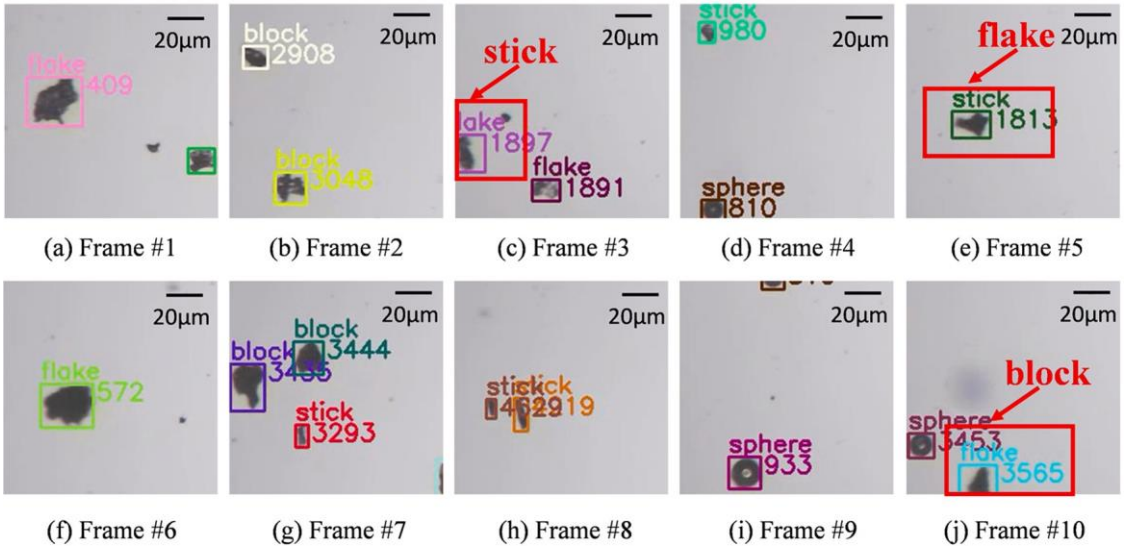

Fig. 10. Recognition results of the HIVE-COTE2.0 method.

training and their distribution is shown in Table 2.

After training the classifier, videos of moving wear debris were captured to test the performance of the proposed dynamic recognition method. There are 158 debris samples were captured for testing and their distribution also shown in Table 2. The wear debris whose equivalent diameters are larger than 10 μm is determined as target objects for counting and recognition. Fig. 8 shows the monitor system interface of moving wear debris. When the wear debris move in the field of view of the camera multi-view images are captured for target debris detection and tracking. When the debris pass through the field boundary dividing line, debris counting is performed and then the debris is recognized based on the image sequence features.

4.2. *Experimental results*

To assess the performance of the proposed method, other time series classification methods including Inception Time [37], HIVE-COTE2.0 [38], and MultiRocket [39] are employed for comparative analysis.

4.2.1. *Qualitative analysis*

The dynamic recognition results obtained from the four classification algorithms are shown in Fig. 9 — 12. For ease of visualisation, the partial regions of debris recognition are cropped. It is observed that the four methods can be used to identify the block, stick, sphere, and flake wear debris under motion conditions. However, identification errors are still noticed. In Fig. 9(c) and Fig. 9(e) of the Inception Time providing results, the stick debris (ID 1897) is identified as flake, and the flake debris (ID 1813) is identified as stick. Meanwhile, the stick debris (ID 1897) is determined as flake by HIVE-COTE2.0; flake debris with ID 1813 is determined as stick by the MultiRocket method, as shown in Fig. 10 and Fig. 11, respectively. Besides, in Fig. 10(j), Fig. 11(j), and Fig. 12(j), the HIVE-COTE2.0, the MultiRocket, and the proposed method falsely detected the block wear debris with ID 3565 as flake type. This is because flake-like and block-like debris have similar contours especially when they are blurry.

4.2.2. *Quantitative analysis*

For further analysis of the performance of different debris recognition algorithms, the precision, recall and F-measure values are utilised to

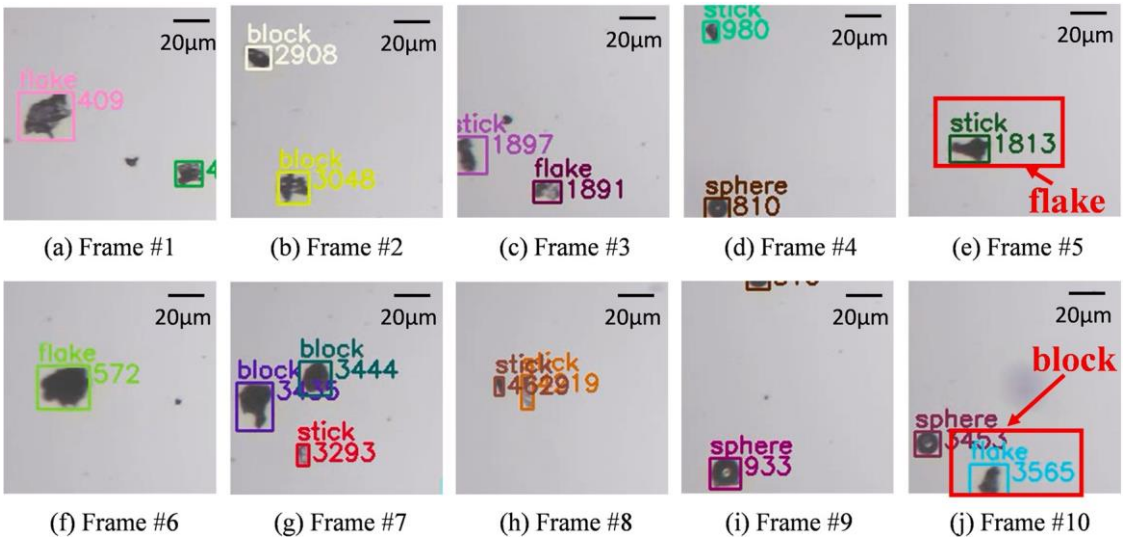

Fig. 11. Recognition results of the MultiRoket method.

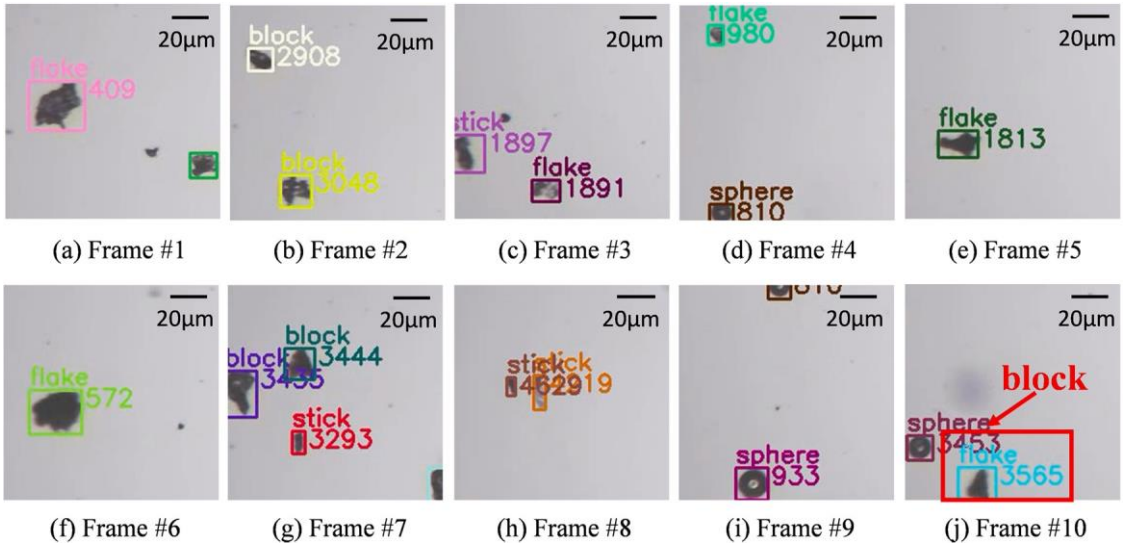

Fig. 12. Recognition results of the proposed method.

evaluate the recognition accuracy. The definitions are shown in Eqs. (7–9). The *Precision* indicates how many positive samples are correctly predicted, and the *Recall* indicates the probability of being predicted as positive samples among all samples.

$$Precision = \frac{TP}{TP + FP} \tag{7}$$

$$Recall = \frac{TP}{TP + FN} \tag{8}$$

$$F-measure = 2 \times \frac{Precision \times Recall}{Precision + Recall} \tag{9}$$

where *TP* represents the number of positive samples that are recognized as positive ones, *FP* is the number of negative samples that are recognized as positive ones, and *FN* is the number of positive samples that are recognized as negative ones.

The debris recognition results of different methods are shown in Table 3. It can be seen that the F-measure values obtained by the Inception Time, the HIVE-COTE2.0, and the MultiRocket are 85.44%, 82.91%, and 74.05%, respectively. The proposed method shows the highest accuracy, Precision (90.51%), Recall (90.51%), and F-measure (90.51%) of all wear debris, as compared with the other three methods. For the failing cases, false recognition can also be caused by the low resolution of image frames, the similar contour information of different viewing images, and the insufficient image frames of irregular debris. This indicates that the established probability-weighted ensemble SVM is more suitable for the dynamic recognition of artificial joint wear debris from lubricants. In addition, moving wear debris imaging is also needed to improve the image quality for feature extraction.

4.2.3. *Efficiency analysis*

To evaluate the capability of on-line wear debris monitoring, the processing efficiencies of four recognition methods are tested. The computer setup contains a Windows 10, 64-bit operating system, a CPU of Core i9–9900 K, 3.6 GHz, 32 GB RAM, and a GPU of 8 GB GeForce RTX 2080. The running times of the four debris recognition methods are shown in Table 4. It shows that all the algorithms have close efficiency. The processing rate of the proposed method is 10.5 fps, which is slightly faster than that of the HIVE-COTE2.0 (9.1 fps) and the MultiRocket (9.9 fps). The Inception Time achieves the highest efficiency of 11.9 fps

Table 3
The debris recognition results of different methods.

Model	Debris type	*TP*	*FP*	*FN*	*Precision*	*Recall*	*F-measure*
Inception Time	Block	76	4	13	95.00%	85.39%	89.94%
	Stick	25	11	1	69.44%	96.15%	80.65%
	Sphere	10	0	1	100.00%	90.91%	95.24%
	Flake	24	8	8	75.00%	75.00%	75.00%
	Overall	135	23	23	85.44%	85.44%	85.44%
HIVE-COTE2.0	Block	76	7	13	91.57%	85.39%	88.37%
	Stick	25	10	1	71.43%	96.15%	81.97%
	Sphere	10	0	1	100.00%	90.91%	95.24%
	Flake	20	10	12	66.67%	62.50%	64.52%
	Overall	131	27	27	82.91%	82.91%	82.91%
MultiRocket	Block	68	9	21	88.31%	76.40%	81.93%
	Stick	23	17	3	57.50%	88.46%	69.70%
	Sphere	11	5	0	68.75%	100.00%	81.48%
	Flake	15	10	17	60.00%	46.88%	52.63%
	Overall	117	41	41	74.05%	74.05%	74.05%
Proposed	Block	79	4	10	95.18%	88.76%	91.86%
	Stick	25	6	1	80.64%	96.15%	87.72%
	Sphere	9	0	2	100.00%	81.82%	90.00%
	Flake	30	5	2	85.71%	93.75%	89.55%
	Overall	143	15	15	90.51%	90.51%	90.51%

Table 4
Comparison of operating efficiency of different models.

Method	Inception Time	HIVE-COTE2.0	MultiRocket	Proposed method
Running time	84 ms	110 ms	101 ms	95 ms
Efficiency	11.9 fps	9.1 fps	9.9 fps	10.5 fps

because its program processing can be accelerated using the GPU. To guarantee the efficiency of moving wear debris processing, the video is captured for 5 min and then paused for 10 min.

5. Conclusion

A method is proposed for dynamic identification of multi-view feature sequences of artificial joint wear debris based on probability-weighted ensemble SVM. The multi-view feature sequence of wear debris is obtained by detecting and tracking the objects in videos, whereby the feature change curve is then extracted. The curve is classified by the probability-weighted integrated SVM algorithm, and then the corresponding types of wear debris (block, stick, sphere, and flake) are obtained. The method is tested with a large number of abrasive wear samples and compared against reliable time series classifiers. The experimental results show that the proposed method can obtain better classification performance. Moreover, the method also shows a faster running speed, which suggests an alternative solution for the online condition monitoring of wear debris.

Declaration of Competing Interest

The authors declare the following financial interests/personal relationships which may be considered as potential competing interests: Yeping Peng reports financial support was provided by National Natural Science Foundation of China. Yeping Peng reports financial support was provided by Science and Technology Planning Project of Shenzhen Municipality.

Data Availability

Data will be made available on request.

Acknowledgements

This research was funded by the National Natural Science Foundation of China (Grant No. 51905351) and the Science and Technology Planning Project of Shenzhen Municipality, China (Grant No. JCYJ20190808113413430).

Statement of Originality

1) The paper has not been published previously, that it is not under consideration for publication elsewhere, and that if accepted it will not be published elsewhere in the same form, in English or in any other language, without the written consent of the publisher.
2) The paper does not contain material which has been published previously, by the current authors or by others, of which the source is not explicitly cited in the paper.

References

[1] de Kouchkovsky DA, Ghosh S, Rothlin CV. Induction of sterile type 2 inflammation. Nat Mater 2019;18:193–4.
[2] Nine MJ, Choudhury D, Hee AC, Mootanah R, Abu Osman NA. Wear debris characterization and corresponding biological response: artificial hip and knee joints. Materials 2014;7:980–1016.
[3] Liu H, Ge SR, Cao S, Wang S. Comparison of wear debris generated from ultra high molecular weight polyethylene in vivo and in artificial joint simulator. Wear 2011; 271:647–52.
[4] McMullin BT, Leung M-Y, Shanbhag AS, McNulty D, Mabrey JD, Agrawal CM. Correlating subjective and objective descriptors of ultra high molecular weight wear particles from total joint prostheses. Biomaterials 2006;27:752–7.
[5] Song J, Chen F, Liu Y, Wang S, He X, Liao Z, Mu X, Yang M, Liu W, Peng Z. Insight into the wear particles of PEEK and CFRPEEK against UHMWPE for artificial cervical disc application: Morphology and immunoreaction. Tribology Int 2020; 144:106093.
[6] Li J, Wang K, Li Z, Tu J, Jin G, Su J, Zhai B. Mechanical tests, wear simulation and wear particle analysis of carbon-based nanomultilayer coatings on Ti6Al4V alloys as hip prostheses. RSC Adv 2018;8:6849–57.
[7] Jia F, Wei H. FWDNet: a novel recognition network for ferrography wear debris image analysis. Wirel Commun Mob Comput 2022;2022:6511235.
[8] Yuan W, Chin K, Hua M, Dong G, Wang C. Shape classification of wear particles by image boundary analysis using machine learning algorithms. Mech Syst Signal Process 2016;72–73:346–58.
[9] Yan X, Xu X, Sheng C, Yuan C, Li Z. Intelligent wear mode identification system for marine diesel engines based on multi-level belief rule base methodology. Meas Sci Technol 2018;29:015110.
[10] Peng P, Wang J. Analysis of oxide wear debris using ferrography image segmentation. Ind Lubr Tribology 2019;71:901–6.
[11] Wang J, Liu X, Wu M, Wang X. Direct detection of wear conditions by classification of ferrograph images. J Braz Soc Mech Sci Eng 2020;42:152.
[12] Sun K, Liu X, Chen G, Wang J. Wer Debris recognition and quantification in ferrography images by instance segmentation. Tribology Trans 2022;65:508–18.

[13] Peng Y, Cai J, Wu T, Cao G, Kwok N, Peng Z. WP-DRnet: a novel wear particle detection and recognition network for automatic ferrograph image analysis. Tribology Int 2020;151:106379.
[14] Fan S, Zhang T, Guo X, Wulamu A. FFWR-Net: A feature fusion wear particle recognition network for wear particle classification. J Mech Sci Technol 2021;35: 1699–710.
[15] Fan H, Gao S, Zhang X, Cao X, Ma H, Liu Q. Intelligent recognition of ferrographic images combining optimal CNN with transfer learning introducing virtual images. IEEE Access 2020;8:137074–93.
[16] Peng P, Wang J. Wear particle classification considering particle overlapping. Wear 2019;422:119–27.
[17] Hu X, Song J, Liao Z, Liu Y, Gao J, Menze B, Liu W. Morphological residual convolutional neural network (M-RCNN) for intelligent recognition of wear particles from artificial joints. Friction 2022;10:560–72.
[18] Wang S, Wu T, Wang K, Peng Z, Kwok N, Sarkodie-Gyan T. 3-D Particle surface reconstruction from multiview 2-D images with structure from motion and shape from shading. IEEE Trans Ind Electron 2021;68:1626–35.
[19] Wu H, Kwok N, Liu S, Wu T, Peng Z. A prototype of on-line extraction and three-dimensional characterisation of wear particle features from video sequence. Wear 2016;368:314–25.
[20] Peng Y, Wu Z, Cao G, Wang S, Wu H, Liu C, Peng Z. Three-dimensional reconstruction of wear particles by multi-view contour fitting and dense point-cloud interpolation. Measurement 2021;181:109638.
[21] Peng Y, Wu T, Wang S, Du Y, Kwok N, Peng Z. A microfluidic device for three-dimensional wear debris imaging in online condition monitoring. Proc Inst Mech Eng Part J-J Eng Tribology 2017;231:965–74.
[22] Wu T, Peng Y, Wang S, Chen F, Kwok N, Peng Z. Morphological feature extraction based on multiview images for wear debris analysis in on-line fluid monitoring. Tribology Trans 2017;60:408–18.
[23] Peng Y, Wu T, Cao G, Huang S, Wu H, Kwok N, Peng Z. A hybrid search-tree discriminant technique for multivariate wear debris classification. Wear 2017;392: 152–8.
[24] Wang S, Wu T, Yang L, Kwok N, Sarkodie-Gyan T. Three-dimensional reconstruction of wear particle surface based on photometric stereo. Measurement 2019;133:350–60.
[25] Peng Y, Cai J, Wu T, Cao G, Kwok N, Zhou S, Peng Z. Online wear characterisation of rolling element bearing using wear particle morphological features. Wear 2019; 430:369–75.
[26] Zivkovic Z. Improved adaptive Gaussian mixture model for background subtraction. Proc 17th Int Conf Pattern Recognit 2004:28–31.
[27] Wojke N., Bewley A., Paulus D. Simple online and realtime tracking with a deep association metric. 2017 24th IEEE International Conference on Image Processing (ICIP), 2017: 3645–3649.
[28] Wang J, Yin C. A fast algorithm for computing the Fourier spectrum of a fractional period. J Comput Biol 2021;28:269–82.
[29] Yang J, Zhang H, Peng G. Time-domain period detection in short-duration videos. Signal Image Video Process 2016;10:695–702.
[30] Large J, Lines J, Bagnall A. A probabilistic classifier ensemble weighting scheme based on cross-validated accuracy estimates. Data Min Knowl Discov 2019;33: 1674–709.
[31] Lingras P, Butz C. Rough set based 1-v-1 and 1-v-r approaches to support vector machine multi-classification. Inf Sci 2007;177:3782–98.
[32] Platt J. Probabilistic outputs for support vector machines and comparisons to regularized likelihood methods. Adv Large Margin Classif 1999;10:61–74.
[33] Wu T, Lin C, Weng R. Probability estimates for multi-class classification by pairwise coupling. J Mach Learn Res 2004;5:975–1005.
[34] Friedman J. Another approach to polychotomous classification. Tech Rep Stat Dep Stanf Univ 1996.
[35] Yang W, He X, Li H, Dong J, Chen W, Xin H, Jin Z. A tribological investigation of SLM fabricated TC4 titanium alloy with carburization pre-treatment. Ceram Int 2020;46:3043–50.
[36] Pinto-Borges H, Pinto J, Carvalho O, Henriques B, Silva F, Gomes J, Ramos A, Souza JCM. Stresses, friction, and wear on different materials and design for temporomandibular joint total joint replacement (TMJ TJR). Tribology Int 2023; 178:108051.
[37] Fawaz HI, Lucas B, Forestier G, Pelletier C, Schmidt DF, Weber J, Webb GI, Idoumghar L, Muller P-A, Petitjean F. InceptionTime: Finding AlexNet for time series classification. Data Min Knowl Discov 2020;34:1936–62.
[38] Middlehurst M, Large J, Flynn M, Lines J, Bostrom A, Bagnall A. HIVE-COTE 2.0: A new meta ensemble for time series classification. Mach Learn 2021;110:3211–43.
[39] Tan C, Dempster A, Bergmeir C, Webb GI. MultiRocket: Multiple pooling operators and transformations for fast and effective time series classification. arXiv Prepr arXiv 2021;210200457.